Chemical Geology 712 (2026) 123428

Contents lists available at ScienceDirect

Chemical Geology

journal homepage: www.elsevier.com/locate/chemgeo

Antimony uptake by iron(III) (oxyhydr)oxide nanoparticles: Roles of particle size and Ni(II) co-sorption

Xiyang Xu [a], Biao Wan [a,b], Kerstin Hockmann [c], Valerie A. Schoepfer [d], Andreas Kappler [a], Muammar Mansor [a,*], Prachi Joshi [a,e,*]

[a] Department of Geosciences, University of Tübingen, 72076 Tübingen, Germany
[b] College of Resources & Environment, Huazhong Agricultural University, 430070 Wuhan, China
[c] Institute of Earth and Environmental Sciences, University of Freiburg, 79104 Freiburg, Germany
[d] Department of Geological Sciences, University of Saskatchewan, S7N 5E2 Saskatoon, Canada
[e] Swiss Federal Institute for Forest, Snow and Landscape Research, 8903 Birmensdorf, Switzerland

ARTICLE INFO

Editor: Yuanzhi Tang

Keywords:
Iron (oxyhydr)oxides
Nanoparticles
Antimony
Adsorption
Co-sorption

ABSTRACT

Antimony (Sb) is a priority environmental pollutant, with mobility and fate that are tightly linked to sorption reactions with iron(III) (oxyhydr)oxide minerals. However, the impact of particle size and co-existing cations (e.g., Ni^{2+}, a representative divalent cation commonly present in Sb-mining-impacted environments) on Sb(V) adsorption capacity and retention mechanisms remains poorly understood. In this study, we synthesized goethite and hematite of varying particle sizes, performed batch Sb(V) adsorption and Ni^{2+}–Sb(V) co-sorption experiments, and characterized samples using micro X-ray diffraction (μ-XRD), scanning and transmission electron microscopy (SEM/TEM), ^{57}Fe Mössbauer spectroscopy, and extended X-ray absorption fine structure (EXAFS) spectroscopy. Our findings reveal that (i) Sb(V) adsorption capacities ranged from 2.5 to 55.7 mg/g, with higher affinities observed for smaller particles and for goethite relative to hematite, even after accounting for surface area, (ii) the presence of Ni^{2+} markedly enhanced Sb(V) adsorption onto both goethite and hematite, with adsorption capacities increasing by 16–89% as particle size decreased, and (iii) the retention mechanism for Sb(V) adsorption changed from being dominated by edge-sharing inner-sphere complexes to enhanced electrostatic interactions and the likely formation of ternary surface complexes in the presence of Ni^{2+}. These findings demonstrate that nanoparticulate goethite and hematite minerals possess even higher potential for Sb(V) removal in complex multi-pollutant systems than previously suggested. Moreover, the dominance of inner-sphere binding and the likely formation of ternary surface complexes suggest that the adsorbed Sb(V) is relatively stable, favoring long-term sequestration in Fe-rich environments.

1. Introduction

Iron(III) (oxyhydr)oxides (a term used here to collectively refer to goethite and hematite) are ubiquitous in a diverse range of environmental, geological, planetary, and technological settings (Hochella Jr et al., 2008; Navrotsky et al., 2008; Von Der Heyden et al., 2019). Depending on environmental conditions during formation, the formed iron(III) (oxyhydr)oxides display a broad distribution of particle sizes, from nm-scale to mm-scale (Hochella Jr et al., 2008). Across this size spectrum, mineral reactivities and physicochemical properties can vary with size even without a phase transformation (Hochella Jr, 2002; Gilbert and Banfield, 2005). These variations are due to differences in surface to area ratios, crystal shape, surface topography, and bonding environments as well as quantum mechanistic effects (Hochella Jr et al., 2008). Therefore, the reactivity of nanoscale iron(III) (oxyhydr)oxides, such as surface sorption behavior, is difficult to predict based on comparison with their bulk counterparts.

Antimony (Sb) has been declared as a priority environmental pollutant by both the United States Environmental Protection Agency and the European Union, due to its chronic toxicity (Filella et al., 2002a; Filella et al., 2009a). In natural aquatic environments, Sb occurs mainly in the +III and +V redox states. Under oxic to slightly reducing

* Corresponding authors at: Department of Geosciences, University of Tübingen, 72076 Tübingen, Germany; Swiss Federal Institute for Forest, Snow and Landscape Research, 8903 Birmensdorf, Switzerland.
E-mail addresses: muammar.mansor@uni-tuebingen.de (M. Mansor), prachi.joshi@wsl.ch (P. Joshi).

https://doi.org/10.1016/j.chemgeo.2026.123428
Received 10 December 2025; Received in revised form 9 April 2026; Accepted 14 April 2026
Available online 15 April 2026

conditions, Sb(V), mainly as $Sb(OH)_6^-$, is the dominant redox Sb species (Filella et al., 2002b; Wilson et al., 2010; He et al., 2019). The environmental behavior, mobility and fate of Sb species have been shown to be tightly linked to sorption or co-precipitation reactions with iron(III) (oxyhydr)oxides (Sun et al., 2023; Burton et al., 2019; Guo et al., 2014; Ritchie et al., 2013). For example, Guo et al. (Guo et al., 2014) reported that Sb(V) adsorption capacities on goethite and hematite at pH 7 range from 7.5 to 11.1 mg/g, while Sun et al. (Sun et al., 2023) observed a similar capacity of 6.9 mg/g for Sb(V) retention on goethite. Beyond the absolute adsorption capacity, the type of surface complexes formed also plays a critical role in Sb(V) retention, as some surface complexes are associated with weaker bonding environments and thus easier release of Sb to the aqueous phase compared to other complexes. Sun et al. (Sun et al., 2023) identified nine distinct Sb(V) surface complexes on various goethite crystal planes. Similarly, Yan et al. (Yan et al., 2022) revealed that Sb(V) adsorption depend on both Sb(V) concentration and hematite surface facets, which together control the molecular Sb(V) surface complexes on hematite. Despite extensive studies on Sb(V) adsorption at macro- and microscale levels, the influence of particle size of the sorbents on Sb(V) adsorption capacity and retention mechanisms remains insufficiently understood; often, the size is not reported or differences in sizes have not been investigated, thus warranting systematic investigation. Size-dependent reactivity has been shown to play critical roles in reduction, adsorption and oxidation reactions (Xu et al., 2025; Madden et al., 2006; Madden and Hochella Jr, 2005). For example, nanoscale iron(III) (oxyhydr)oxides exhibit enhanced adsorption affinity and altered binding mechanisms for Cu^{2+} and Cr(VI) (Madden et al., 2006; Xiao et al., 2015). Without understanding how Sb(V) retention varies as a function of particle size, predictions of Sb mobility, bioavailability, and long-term stability in natural and contaminated environments remain poorly constrained.

While abundant studies have investigated the adsorption capacity and retention mechanisms of individual Sb(V), antimony rarely exists by itself in natural systems, limiting the environmental relevance of such investigations. Instead, it commonly co-occurs with other dissolved ions, including cationic species (e.g., Zn^{2+}, Pb^{2+}, Ca^{2+}, Ni^{2+}) and anionic species (e.g., AsO_4^{3-}, CO_3^{2-}) (Khan et al., 2019; Jurkovič et al., 2019; Palmer et al., 2015; Trois et al., 2007; Barker et al., 2020; Majzlan et al., 2011). Specifically, Jurkovič et al. (Jurkovič et al., 2019) reported that highly contaminated soils with pH ranges of 3.5–7 and high metal(loid) load, such as antimony (Sb), arsenic (As), lead (Pb), and zinc (Zn), were observed at the abandoned Sb-deposit in eastern Slovakia. Similarly, Khan et al. (Khan et al., 2019) revealed that increased metal mining in the Arctic region has resulted in elevated loads of arsenic (As), antimony (Sb), and nickel (Ni) to recipient surface or groundwater systems. Although the coexistence of contaminants in the environment is expected, there have been only a few studies examining how coexistence affects overall adsorption capacity and underlying mechanisms (Kumar et al., 2025; Song et al., 2022; Shi et al., 2021). For instance, Song et al. (Song et al., 2022) and Jiang et al. (Jiang et al., 2019) demonstrated that Ca^{2+} enhances Sb(V) adsorption on goethite and TiO_2, either increasing the proportion of bidentate corner-sharing complexes through electrostatic interactions or forming Ca–Sb(V)–TiO_2 ternary complexes, respectively. To date, the combined effects of particle size and co-existing cations (specifically Ni^{2+} in our study, a representative divalent cation that commonly co-occurs with Sb in mining-impacted environments and does not form precipitates with dissolved Sb species) on Sb(V) adsorption capacity and retention mechanisms have received little attention.

In this study, we systematically investigated the adsorption capacity and retention mechanisms of Sb(V) on goethite and hematite as a function of particle size using a combination of batch adsorption and co-sorption experiments. The work had three specific objectives: (i) To assess the adsorption capacity and behavior of Sb(V) on goethite and hematite across varying particle sizes, (ii) To evaluate the influence of the co-existing divalent cation Ni^{2+} on the adsorption capacity and behavior of Sb(V) as a function of particle size, (iii) To investigate the (molecular scale) mechanisms underlying the retention of Sb(V) in the absence and presence of Ni^{2+} and as a function of particle size. To achieve these objectives, we synthesized goethite and hematite with different particle sizes in the nanometer to micrometer range. Then, we conducted batch Sb(V) adsorption and co-sorption experiments in the absence and presence of Ni^{2+}. We characterized the solid-phase samples using micro X-ray diffractometry (μ-XRD), scanning/transmission electron microscopy (SEM/TEM), ^{57}Fe Mössbauer spectroscopy, and extended X-ray absorption fine structure (EXAFS) spectroscopy, and quantified the concentrations of Sb and Ni through inductively coupled plasma mass spectrometry (ICP-MS). The findings of this study advance our understanding of the adsorption capacity and retention mechanisms of Sb(V) on iron(III) (oxyhydr)oxides across varying particle sizes, with implications for their behavior in natural environments.

2. Materials and methods

2.1. Synthesis and characterization of iron(III) (oxyhydr)oxide minerals with varying particle sizes

Goethite (Gt) and hematite (Hm) with varying particle sizes were synthesized following on our previous methods (Xu et al., 2025; Xu et al., 2026). Particle size was controlled through hydrolysis and aging methods under different pH, temperature, initial Fe(III) concentration, and reaction time conditions, with detailed procedures provided in the SI, Section S1. The synthesized minerals are referred to as Large Gt, Medium Gt, Small Gt, and Large Hm, Medium Hm, Small Hm based on their respective particle size. The mineralogy of the synthesized iron(III) (oxyhydr)oxides were determined using micro-X-ray diffraction (μ-XRD) and ^{57}Fe Mössbauer spectroscopy. The morphologies and particle size distributions of the iron(III) (oxyhydr)oxides were characterized using scanning electron microscopy (SEM) and transmission electron microscopy (TEM). The (hydrodynamic) size and surface charge of the iron (III) (oxyhydr)oxides were measured by dynamic light scattering (DLS, Malvern Zetasizer Nano ZS). Details regarding the characterization are provided in the SI, Section S1.

2.2. Adsorption and co-sorption experiments

Antimony adsorption onto goethite and hematite in the presence and absence of Ni^{2+} was studied in batch experiments. First, iron(III) (oxyhydr)oxide suspensions (1 g/L) were prepared in a solution containing 5 mM $NaHCO_3$ as buffer (pH 6.5) and 10 mM NaCl, and equilibrated overnight to stabilize the pH. On the following day, the suspensions were readjusted to pH 6.5 using 0.1 M HCl or NaOH, if necessary. We selected pH 6.5 to simulate the circumneutral conditions typical of natural water bodies contaminated with Sb (Filella et al., 2009b). $NaHCO_3$ was used as a carbonate buffer representative of the carbonate-rich environments often associated with Sb ores (Filella et al., 2009b). After pH adjustment, 15 mL of the suspension was transferred into 25 mL serum bottles. Stock solutions of Sb (as $KSb(OH)_6$) were first added to the suspensions, followed immediately by Ni (as $NiCl_2$) in case of co-sorption, to achieve target concentrations ranging from 10 to 1200 μM Sb(V) and 0 to 600 μM Ni(II), maintaining a 1:1 Sb:Ni molar ratio in the co-sorption systems. Ni was chosen due to its common co-occurrence with Sb in mining sites (Khan et al., 2019; Jurkovič et al., 2019; Palmer et al., 2015; Trois et al., 2007). The selected concentration ranges and fixed molar ratio are environmentally relevant to contaminated waters and soils in Sb mining-impacted regions (Khan et al., 2019; Jurkovič et al., 2019; Palmer et al., 2015; Trois et al., 2007; Majzlan et al., 2011). In addition, the systems remain undersaturated with respect to $Ni(OH)_2$, $NiCO_3$, and potential Ni—Sb precipitates under the experimental concentrations (Arai, 2008; Hummel and Curti, 2003). The bottles were sealed with rubber stoppers and aluminum caps, and the suspensions were allowed to react for 48 h. During this period, the

bottles were placed on a rolling shaker at 65 rpm and covered with aluminum foil to minimize photochemical reactions. At the end of the reaction period, the final pH of the quiescent suspensions was measured and found to be stable within ±0.3 pH units. The suspensions were centrifuged at 12,100 ×*g* for 10 min, and the supernatants were filtered through 0.22 μm mixed cellulose ester (MCE) membrane syringe filters. Total Sb and Fe concentrations in the supernatants were analyzed by inductively coupled plasma mass spectrometry (ICP-MS, Agilent 7900, USA) following acidification to 2% HNO_3. The standard deviation of all element measurements was <10%.

In this study, Sb(V) was used to represent the aqueous and mineral-associated antimonate species, while Ni^{2+} and Ni(II) were used to denote the divalent nickel species in the dissolved and mineral-associated phases, respectively. Under the initial reaction conditions in the presence of Ni^{2+}, the co-sorption systems were undersaturated with respect to $Ni(OH)_2$ (am), β-$Ni(OH)_2$, and $NiCO_3$ based on solubility calculations using the thermodynamic solubility constants (log K_{sp}: −12.89, −10.8, and − 11.2, respectively) (Arai, 2008; Hummel and Curti, 2003).

2.3. Adsorption models

In this study, Sb(V) adsorption on goethite and hematite was modeled using both the Langmuir and the Freundlich isotherms.

The Langmuir model was used to simulate the monolayer adsorption, as shown in the following equation (Langmuir, 1918):

$$q_e = \frac{q_m K_L C_e}{1 + K_L C_e} \quad (1)$$

where q_m (mg/g) is the maximum monolayer adsorption capacity; K_L (L/mg) is the adsorption equilibrium constant; and q_e (mg/g) is the amount adsorbed at equilibrium concentration C_e (mg/L).

An important parameter related to the Langmuir model is the separation factor or equilibrium parameter, denoted as R_L, which is used to check if adsorption is favorable or unfavorable (Gunawardene et al., 2021; Hall et al., 1966). Mathematically, it can be shown as:

$$R_L = \frac{1}{1 + K_L C_o} \quad (2)$$

where K_L and C_o are the Langmuir adsorption equilibrium constant and the initial concentration of Sb(V), respectively. In general, $R_L < 1$ indicates that adsorption is favorable; $R_L \sim 0$ indicates that adsorption is irreversible; $R_L = 1$ indicates that the adsorption isotherm is linear, and $R_L > 1$ corresponds to unfavorable adsorption.

The Freundlich equation is an empirical adsorption model that can be expressed as the following equation (Freundlich, 1907):

$$q_e = K_d C_e^{\,1/n} \quad (3)$$

where q_e and C_e were defined earlier, K_d is Freundlich constant, and $1/n$ is the adsorption intensity or surface heterogeneity. When $0 < 1/n < 1$, adsorption is considered favorable. Unfavorable adsorption occurs when $1/n > 1$ and is irreversible at $1/n = 1$.

2.4. Sb K-edge XANES and EXAFS analysis

The redox speciation of adsorbed Sb in the absence and presence of co-existing Ni^{2+} was quantified using Sb K-edge X-ray absorption near-edge structure spectroscopy (XANES). Sb K-edge was recorded in fluorescence mode on diluted powders at cryogenic temperatures (80 K) at the BioXAS beamline at Canadian Light Source (CLS) using a Si (220) monochromator. Reference standards included Sb_2O_3, $KSb(OH)_6$ and tripuhyite ($SbFeO_4$; synthesized by heating equimolar amounts of Fe_2O_3 and Sb_2O_3 for 12 h at 973 °C (Martinelli et al., 2002)). The diluted samples and standards were pressed into pellets (7 mm diameter) and mounted on the sample holders. Data were recorded in fluorescence mode using two 32-element Ge detectors with a Zr-filter and Soller slits placed between the detector and the sample to enhance the signal-to-noise ratio. An Sb metal foil (30,491 eV) located downstream of the sample was used for energy calibration, and an Al foil was used to filter the background Fe fluorescence signal. Three replicate spectra were collected per sample. Raw Sb K-edge XANES spectra were merged and exported with the corresponding reference foil spectra. Normalization and background subtraction were performed using the ATHENA software (Ravel and Newville, 2005). The redox state of Sb was determined via linear combination fitting (LCF) of normalized Sb K-edge XANES spectra, using Sb_2O_3 (Sb(III)) and $KSb(OH)_6$ (Sb(V)) as reference standards. Fourier transforms of normalized Sb k^3-weighted $\chi(k)$ data were calculated over a k-range of 3 to 12.5 $Å^{-1}$, using a hanging window function with dk = 1. Least-squares fittings of k^3-weighted extended X-ray absorption fine structure (EXAFS) spectra were performed using Artemis (Ravel and Newville, 2005), with theoretical phase-shift and amplitude functions calculated using the ab initio FEFF6 code (Ankudinov et al., 1998). Scattering paths used to model Sb K-edge EXAFS spectra were extracted from the structures of tripuhyite (Berlepsch et al., 2003). Details regarding Sb K-edge XAS analysis are provided in the SI, section S3.

3. Results and discussion

3.1. Characterization of goethite and hematite nanoparticles

To study the size-dependent adsorption and co-sorption behavior of goethite and hematite toward Sb(V), we synthesized goethite and hematite with a range of different sizes (30–2000 nm for goethite and 10–300 nm for hematite). The identity of the synthesized phases was confirmed using μ-XRD and ^{57}Fe Mössbauer spectroscopy, while size distributions were determined by measuring individual particles in SEM and TEM images.

Reflections indicative of pure goethite and hematite were identified in the μ-XRD patterns (SI, Fig. S1). Widths of the reflections in the μ-XRD patterns increased with decreasing sizes, indicating a lower crystallinity, which was consistent with our previous study (Xu et al., 2025). Additionally, the presence of pure goethite and hematite phases was confirmed by ^{57}Fe Mössbauer spectroscopy (SI, Fig. S2 and Table S1). Differences in Mössbauer fitting parameters between different-sized nanoparticles revealed slight variations in magnetic properties of samples, indicating distortion in the crystal lattice and/or a decrease in particle size. Furthermore, the presence of multiple sextets may be indicative of a distribution of crystallinities within samples (Murad and Cashion, 2011). Collectively, the smaller particle size resulted in lower crystallinity and a distorted lattice, with relatively minor changes in mineral identity.

Particle sizes were determined based on the average size of goethite and hematite particles observed in TEM and SEM images (SI, Fig. S3 and Fig. S4). The iron(III) (oxyhydr)oxide minerals synthesized in this study are referred to heretofore as Large Gt (acicular nanoparticles with a mean length ± width of 2000 ± 350 nm), Medium Gt (acicular nanoparticles, 90 ± 10 nm), and Small Gt (short rod-like nanoparticles, 30 ± 10 nm); as well as Large Hm (pseudo-hexagon platelets with a mean diameter of 300 nm), Medium Hm (pseudo-hexagon platelets, 40 nm), and Small Hm (pseudo-hexagon platelets, 10 nm).

3.2. Size-dependent individual Sb(V) adsorption

Macroscopic adsorption results of individual Sb(V). To investigate the size-dependent adsorption capacity of goethite and hematite for Sb(V), batch adsorption experiments were conducted using iron(III) (oxyhydr)oxide particles of varying sizes at pH 6.5. The amount of Sb(V) adsorbed by the iron(III) (oxyhydr)oxides in the experiments gradually increased with increasing initial Sb concentration and eventually

reached a plateau within 48 h incubation (Fig. 1A, C). Notably, the adsorption capacity of the smaller particles was consistently higher than that of the larger particles, regardless of the mineral type. The adsorption data are better fit by the Langmuir model (Table S2; $R^2 = 0.95–0.99$ for goethite, 0.67–0.98 for hematite) than the Freundlich model (Table S2; $R^2 = 0.89–0.95$ for goethite, 0.65–0.94 for hematite). This suggests that Sb(V) adsorption predominantly occurs on homogeneous surfaces with monolayer coverage, which is supported by previous work (Guo et al., 2014; Xi and He, 2013). In addition, it is believed that R_L values lying between 0 and 1 indicate a favorable adsorption process, whereas $R_L > 1$ suggests an unfavorable process, and $R_L \sim 0$ corresponds to irreversible adsorption (Gunawardene et al., 2021; Sari et al., 2007). As shown in SI, Fig. S5, all calculated R_L values fall within the 0–1 range, confirming that the adsorption of Sb(V) onto the iron(III) (oxyhydr)oxides is thermodynamically favorable under the tested conditions. Furthermore, the Freundlich constant $1/n$ values were consistently less than 1, which also implies the favorable and effective sorption of Sb(V) on these iron(III) (oxyhydr)oxides.

The maximum adsorption amount (Fig. 1B, D) was expressed as the surface area-normalized adsorption capacity, obtained by dividing the Langmuir-derived maximum adsorption capacity (q_m) by the BET surface area (SI, Table S4). The adsorption capacity of Sb(V) ranged from 1.13 to 2.28 μmol/m^2 for goethite and from 1.31 to 1.81 μmol/m^2 for hematite. These values were comparable to the previous reported value of 0.5 to 2.3 μmol/m^2 for goethite and 0.7 to 4.5 μmol/m^2 for hematite at the identical pH conditions (Sun et al., 2023; Guo et al., 2014; Xi and He, 2013). In contrast to previous work, however, here we can directly relate the adsorption capacity to the particle size, which was missing till now. In addition, a clear trend of increasing adsorption capacity with decreasing particle size was observed, consistent with previous studies reporting enhanced adsorption of other trace elements onto smaller particles even after accounting for surface area differences (Madden et al., 2006; Barton et al., 2011). This observed size-dependent adsorption capacity may be attributed to differences in nanoparticle related intrinsic properties, such as surface charge, defect sites, and undercoordinated Fe vacancies (Hou et al., 2022; Notini et al., 2018). Additionally, Medium and Small Gt exhibited higher adsorption capacities for Sb(V) compared to Medium and Small Hm. The Large Gt and Hm exhibited similar adsorption capacities. This trend was supported by

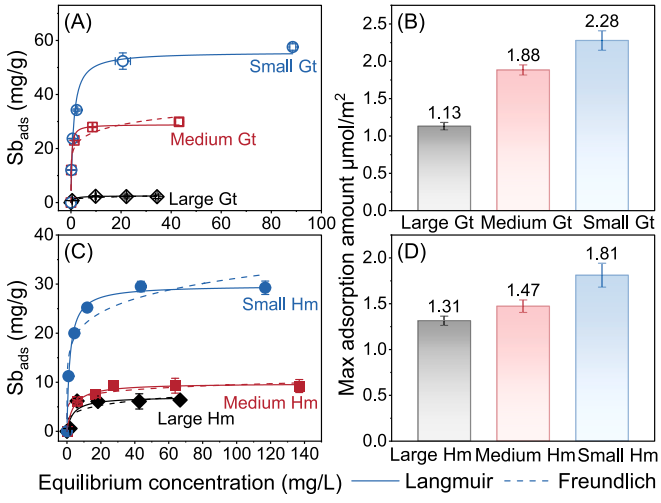

Fig. 1. Adsorption isotherms and maximum adsorption amount per unit surface area for Sb(V) on goethite (A, B) and hematite (C, D) with varying particle sizes. The solid lines in panel A and C represent the fit by the Langmuir model, and the dashed lines in panel A and C denote the fit by the Freundlich model. All adsorption experiments were conducted by reacting Sb with 1 g/L goethite and hematite in a solution containing 10 mM NaCl and 5 mM $NaHCO_3$ at pH 6.5. The initial Sb concentrations ranged from 10 to 1200 μM.

the Langmuir affinity constant (K_L). The tendency for preferential adsorption on goethite may be attributed to the abundance of hydroxyl functional groups, as well as specific mineral edges and defect sites known to enhance surface reactivity (Liu et al., 2014).

Surface charge and aggregation pattern for individual Sb(V) adsorption. In order to discern if surface charge and/or aggregation patterns could explain the surface-area independent higher adsorption by smaller particles, we conducted zeta potential and dynamic light scattering (DLS) measurements. The points of zero charge (PZC) of the synthesized iron(III) (oxyhydr)oxides, determined from zeta potential measurements (SI, Fig. S8), were 9.2, 8.5, and 8.2 for Large, Medium, and Small Gt, and 9.2, 9.0, and 8.0 for Large, Medium, and Small Hm, respectively. These values indicate that all surfaces, in principle, were positively charged at the experimental pH of 6.5. Since Sb(V) exists predominantly as the anion $Sb(OH)_6^-$ under our tested condition (Kumar et al., 2025), electrostatic attraction between the negatively charged antimonate and positively charged mineral surfaces likely contributes significantly to Sb(V) adsorption.

In addition, intensity-weighted size distributions of goethite and hematite suspensions at pH 3 and 6.5 are shown in Fig. 2. At pH 3, far from their point of zero charge (8.0–9.2; see above), the suspensions were relatively well-dispersed, representing sizes close to the primary particle. In contrast, under the experimental pH of 6.5, the hydrodynamic diameters increased substantially, by up to an order of magnitude for Small Gt and Small Hm, indicating extensive aggregation. While such aggregation can influence the reactive surface area, it does not fully account for the observed size-dependent adsorption trends after surface-area normalization. It is important to note that DLS provides only hydrodynamic diameters of aggregates, without information on aggregate morphology or compaction (i.e., loose vs. dense packing), both of which can significantly influence the accessibility of surface sites. Therefore, while electrostatic interactions and aggregation likely contribute to the observed behavior, the consistently higher uptake by smaller particles may also be attributed to their inherently greater surface reactivity, possibly associated with abundant defect sites (Notini et al., 2018) and undercoordinated Fe vacancies (Hou et al., 2022), as supported by the observed structural disorder and lattice distortion in our Mössbauer spectra and XRD patterns (Fig. S1 and S2). The detailed discussion is provided below in Section 3.4, which addresses the mechanisms underlying the size-dependent adsorption and co-sorption behavior.

XAS analysis of Sb(V) surface complexation. To investigate the influence of particle size on Sb(V) binding mechanisms on the iron(III) (oxyhydr)oxides, we performed Sb K-edge XAS measurements with XANES and EXAFS analysis. The redox state of adsorbed Sb throughout adsorption was determined by linear combination fitting (LCF) of Sb K-edge X-ray absorption spectra using Sb(V) ($KSb(OH)_6$) and Sb(III) (Sb_2O_3) reference samples. The normalized XANES spectra of these samples closely resembled those of the pure Sb(V) reference (SI, Fig. S10, Table S6), confirming that Sb remained in the pentavalent state during adsorption. This result, consistent with the oxic experimental conditions and the stability of Sb(V) on iron(III) (oxyhydr)oxide surfaces, validates that subsequent EXAFS analyses reflect the local coordination of Sb(V).

Morlet Wavelet transformations (WT) were employed to resolve the centers of the backscattering wave functions in both *k*-space (Å^{-1}) and *R*-space (Å), providing an effective tool for distinguishing different atoms within a single atomic shell which are difficult to discriminate by shell-by-shell fitting (Funke et al., 2005). The absence of distinct features in the higher-*k* and *R* region ($k > 12$ Å^{-1} and $R + \Delta R > 3$ Å) implies a lack of Sb—Sb backscattering paths in the individual Sb(V) adsorption samples (SI, Fig. S11).

The k^3-weighted Sb K-edge EXAFS spectra and the corresponding Fourier Transform magnitude spectra for individual Sb(V) adsorption onto different-sized iron(III) (oxyhydr)oxides are shown in Fig. 3 and Table S7. The first peak of the EXAFS oscillations is observed at 1.5 Å (phase-shift uncorrected) in each plot (Fig. 3B). This peak was derived

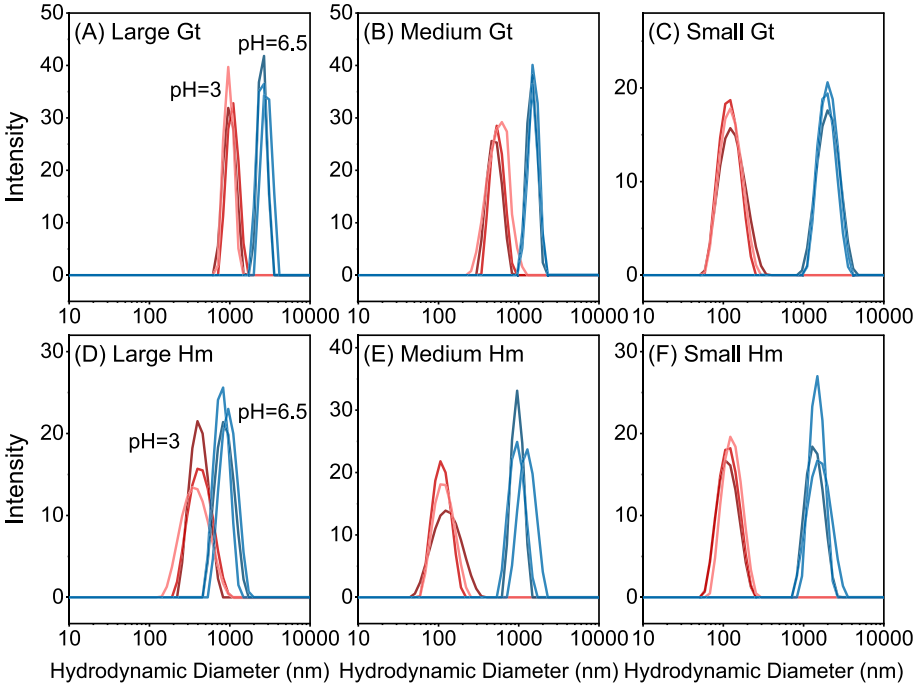

Fig. 2. Hydrodynamic diameter of different-sized iron(III) (oxyhydr)oxides at pH 3 (red) and pH 6.5 (blue). Each line represents a replicate measurement. Panels: (A) Large goethite (Gt), (B) Medium Gt, (C) Small Gt, (D) Large hematite (Hm), (E) Medium Hm, and (F) Small Hm. The data at pH 3 reflect conditions closest to a well-dispersed state. (For interpretation of the references to colour in this figure legend, the reader is referred to the web version of this article.)

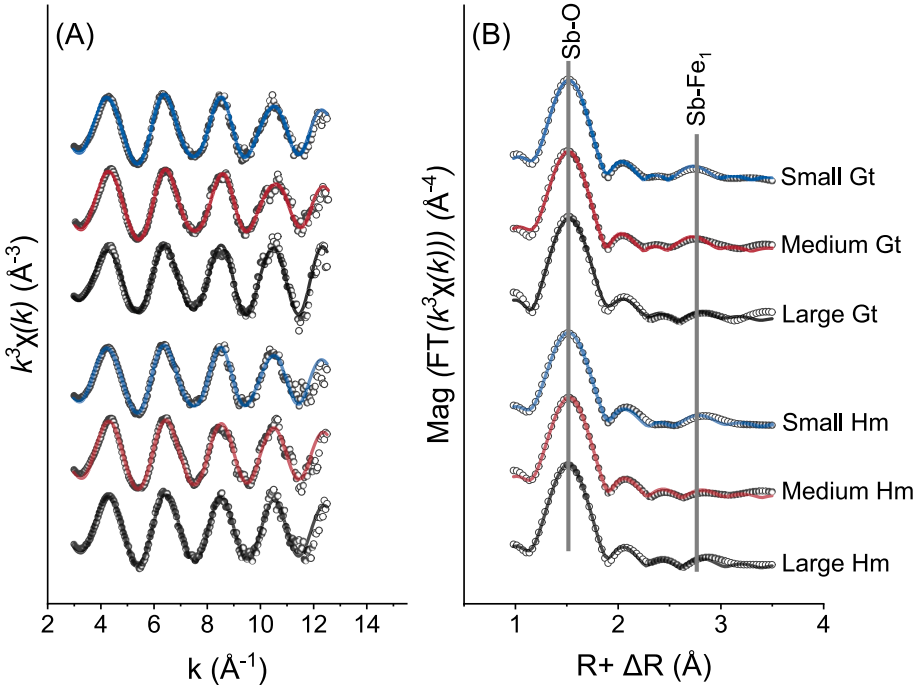

Fig. 3. Antimony K-edge k^3-weighted EXAFS spectra (A) and the corresponding Fourier Transform magnitude spectra (B) for adsorption of individual Sb(V) onto iron (III) (oxyhydr)oxide as a function of particle size. The empty symbols and solid lines show measured data and corresponding shell fits, respectively.

from several O atoms at an average distance of 1.97 Å from the central Sb atom according to the shell-by-shell fitting results (Table S7). The Sb—O distance of 1.97 Å for Sb sorption samples was consistent with previous studies (Burton et al., 2019; Yan et al., 2022; Mitsunobu et al., 2010). For individual Sb(V) adsorption systems, the fitted coordination numbers (CNs) of Sb—O shells were 5.1–6.5, a slight shift from the theoretical CNs (6) of Sb—O for the SbO_6 hexahedron structure, which might arise from the uncertainties associated with the fixed amplitude reduction factor (S_0^2) during fitting (Sun et al., 2023; Yan et al., 2022). Apart from the Sb—O shell, the Sb—Fe_1 shell was obtained in every Sb (V) adsorption sample. Only one Sb—Fe shell with the distance of 3.06–3.12 Å which corresponds to the Sb—Fe distance of edge-sharing complex (Mitsunobu et al., 2010; Verbeeck et al., 2021) was obtained. The coordination numbers (CNs) of the Sb—Fe bond were 0.7–0.9 and

0.3–0.9 for goethite and hematite, respectively, which are comparable to previous Sb adsorbed species (Mitsunobu et al., 2010; Mitsunobu et al., 2013). Notably, the relatively higher coordination numbers (CNs) for goethite relative to hematite, and small particles relative to large particles, further support that goethite phase and smaller particles exhibit a stronger affinity for Sb(V) adsorption. Overall, under pH 6.5 conditions, Sb(V) predominantly forms edge-sharing inner-sphere complexes on iron(III) (oxyhydr)oxides across all particle sizes and mineral types. These configurations represent stronger and more rigid bonding environments than outer-sphere adsorption, likely enhancing Sb(V) immobilization under fluctuating pH conditions.

3.3. Size-dependent co-sorption of Sb(V) with Ni^{2+}

Macroscopic co-sorption trends of Sb(V) with Ni^{2+}. To investigate the size-dependent co-sorption of Sb(V) with Ni^{2+} onto goethite and hematite, batch co-sorption experiments were conducted at pH 6.5 with a fixed Sb(V):Ni(II) molar ratio of 1:1. In the presence of Ni^{2+}, the adsorption isotherms were better fitted by Freundlich model (Table S3; $R^2 = 0.94–0.99$ for goethite, 0.95–0.99 for hematite) than by Langmuir model (Table S3; $R^2 = 0.92–0.97$ for goethite, 0.77–0.91 for hematite). The fitting parameters, including R_L and $1/n$, suggest thermodynamically favorable adsorption and strong affinity of iron(III) (oxyhydr)oxides for Sb(V) in the presence of Ni^{2+}. The better fit of the Freundlich model under co-sorption conditions suggests increased surface heterogeneity, likely arising from the coexistence of multiple binding environments. These include direct adsorption onto mineral surface sites, electrostatic interactions influenced by Ni^{2+} adsorption, and the likely formation of ternary Ni–Sb–Fe surface complexes. These mechanisms are discussed in detail in the following paragraphs.

The maximum adsorption amount of Sb, normalized by BET surface area, exhibited a synergetic enhancement when Sb(V) and Ni^{2+} co-existed in the solution (Fig. 4B, D). Specifically, the adsorption capacity of Sb(V) increased by 18 and 52% for goethite and 16 and 89% for hematite under co-sorption conditions. This observed synergistic behavior of Sb(V) in the presence of Ni^{2+} is likely driven by electrostatic interaction and the potential formation of ternary complexes, and in some cases may involve surface precipitation as Sb oxides, as reported in previous studies (Kumar et al., 2025; Song et al., 2022; Shi et al., 2021; Fan et al., 2016). The underlying mechanisms contributing to this synergistic adsorption will be discussed in detail in subsequent sections.

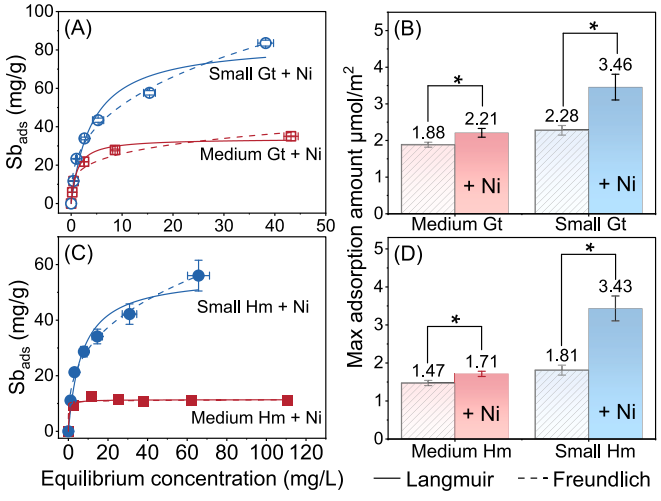

Fig. 4. Adsorption isotherms and maximum adsorption amount per unit surface area for Sb(V) on goethite (A, B) and hematite (C, D) in the presence of Ni^{2+} with varying particle sizes. The solid lines in panel A and C represent the fit by the Langmuir model, and the dashed lines in panel A and C denote the fit by the Freundlich model. The red and blue with hatched pattern in panel B and D represent the maximum adsorption amount of Sb(V) in individual systems, the red and blue and with "+ Ni" inside the columns in panel C and D denote the maximum adsorption amount of Sb(V) in co-existing systems in the presence of Ni^{2+}. Asterisks in panels B and D indicate statistically significant differences between the adsorption and co-sorption groups ($P < 0.05$), as determined by a *t*-test. All co-sorption experiments were conducted by reacting Sb with 1 g/L goethite and hematite in a solution containing 10 mM NaCl and 5 mM $NaHCO_3$ at pH 6.5. Initial Sb concentrations ranged from 100 to 600 μM, with Ni added at a 1:1 M ratio relative to Sb. (For interpretation of the references to colour in this figure legend, the reader is referred to the web version of this article.)

Furthermore, the adsorption isotherms for Ni^{2+} were well fitted by both the Langmuir and Freundlich models (SI, Fig. S6 and Table S5). The adsorption capacity and affinity of Ni^{2+} were consistently lower than those for Sb(V), indicating preferential sorption of Sb(V) compared to Ni^{2+}. To further interpret Sb(V) and Ni^{2+} adsorption behavior, the ratios of the adsorbed Sb(V)/Ni(II) versus the surface coverage (SI, Fig. S7) were plotted. These ratios remained consistently greater than 1, indicating that more Sb(V) than Ni^{2+} was adsorbed onto the mineral surfaces, thereby confirming the preferential adsorption of Sb(V) at initial 1:1 molar ratio between the two elements. Moreover, the relatively stable ratios across increasing surface coverage suggest that Sb(V) and Ni(II) were co-adsorbed in a fixed proportion on the mineral surfaces. This stoichiometric partitioning suggests that the underlying adsorption mechanisms remained consistent with increasing surface loadings. The preferential affinity for anions over cations, such as Sb(V) over Ni^{2+}, observed in this study may be attributed to the surface electrostatic properties of iron(III) (oxyhydr)oxides, discussed below.

Surface charge and aggregation pattern for co-sorption of Sb(V) with Ni^{2+}. To evaluate whether surface charge and/or aggregation could account for the enhanced Sb(V) adsorption capacity in the presence of Ni^{2+}, we performed zeta potential and DLS measurements. Under control conditions (no Sb and no Ni), the iron(III) (oxyhydr)oxide surfaces exhibited mildly positive zeta potential (ζ) values, ranging from +0.6 to +9.1 mV, depending on particle size and mineral phase (Fig. 5). Following individual Sb(V) adsorption, the ζ values shifted markedly to −26.5 to −21.5 mV, indicating a substantial shift to net negative surface charge and consistent with the adsorption of $Sb(OH)_6^-$ onto the mineral surface. In contrast, co-sorption with Ni^{2+} resulted in a partial restoration of surface charge, with ζ values ranging from −8.8 to +11.5 mV. This moderation of surface charge likely results from Ni^{2+} adsorption onto the Sb-modified surfaces, partially neutralizing their negative charge. Such electrostatic rebalancing may decrease repulsive forces

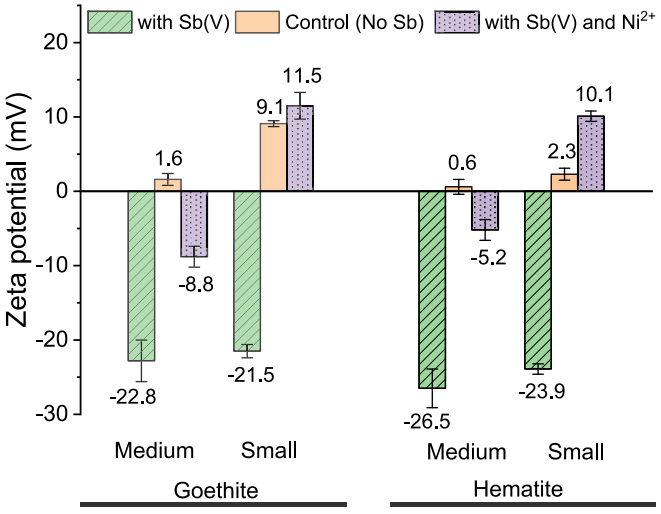

Fig. 5. Zeta potential of iron(III) (oxyhydr)oxides: (i) after 48-h reaction with Sb(V) (ii) under control conditions (no Sb) (iii) after 48-h reaction with Sb(V) and Ni^{2+}. Adsorption of Sb(V) alone leads to a decrease in zeta potential relative to controls, whereas co-sorption with Ni^{2+} results in a higher zeta potential compared to individual Sb(V) adsorption.

between $Sb(OH)_6^-$ and the surface, thereby facilitating further Sb(V) uptake, potentially through the likely formation of ternary surface complexes involving Sb(V), Ni(II), and the iron(III) (oxyhydr)oxide substrate.

In addition, intensity-weighted size distribution of selected goethite and hematite at pH 6.5, after 48-h reaction with Sb(V) and Ni^{2+} or under control conditions (no Sb and no Ni) are shown in SI, Fig. S9. Notably, minerals reacted with Sb(V) and Ni^{2+} displayed shifts toward smaller aggregate sizes compared to controls. This decrease in aggregate size may result in increased exposure of reactive sites and improved accessibility of pore throat within aggregates, thereby enhancing Sb(V) adsorption capacity.

XAS analysis of Sb(V)-Ni^{2+} co-sorption complexes. To investigate the influence of co-existing Ni^{2+} on Sb(V) binding mechanisms on the iron(III) (oxyhydr)oxides, we performed Sb K-edge XAS measurements with XANES and EXAFS analysis. Similar to the individual Sb(V) adsorption systems, co-sorption with Ni^{2+} did not alter the redox state of antimony, which remained as Sb(V) across all particle sizes (SI, Fig. S10; Table S6).

The Morlet wavelet transform (WT) spectra for the co-sorption of Sb (V) with Ni^{2+} on iron(III) (oxyhydr)oxides displayed features similar to those observed for individual Sb(V) adsorption, characterized by dominant Sb—Fe scattering paths and the absence of Sb—Sb backscattering paths (SI, Fig. S12). Notably, the co-sorption samples exhibited comparatively higher fluorescence intensity, suggesting the potential involvement of multiple Sb—Fe scattering paths compared to the spectra from individual Sb(V) adsorption samples (SI, Fig. S12).

The k^3-weighted Sb K-edge EXAFS spectra and the corresponding Fourier Transform magnitude spectra for Sb(V) co-sorption with Ni^{2+} onto different-sized iron(III) (oxyhydr)oxides are shown in Fig. 6 and Table S8. Modelling of the Sb K-edge EXAFS spectra revealed Sb coordination by a first shell comprising 5.9–7.3 O atoms at an inter-atomic distance of 1.97–1.99 Å (Fig. 6, Table S8). This is consistent with an octahedral coordination of Sb(V) by O, thereby supporting the results of our LCF analyses of the XANES spectra (SI, Fig. S10, Table S6). Two Sb—Fe distances were observed in the ranges of 3.03–3.11 Å and 3.52–3.55 Å for both goethite and hematite (Table S8). The first value corresponds to the Sb—Fe distance along the edge-sharing configuration, and the second corresponds to the Sb—Fe distance along the corner-sharing configuration (Burton et al., 2019; Yan et al., 2022; Mitsunobu et al., 2010). The coordination numbers (CNs) of both bonds were 0.5–0.8 and 1.3–2.2, respectively, which are larger than those of Sb—Fe for the individually adsorbed species (Mitsunobu et al., 2010; Mitsunobu et al., 2013). Although incorporation of an Sb—Ni scattering path into the EXAFS model is theoretically possible, distinguishing it at the Sb K-edge is challenging because Ni and Fe, which are adjacent in the periodic table, exhibit nearly identical backscattering amplitudes and phase shifts (Ravel and Newville, 2005; Rehr et al., 1991). Furthermore, direct Sb—Ni interactions are expected to be limited under the studied conditions, as Sb(V) and Ni^{2+} primarily compete for available adsorption sites on the mineral surface. Consequently, most Sb and Ni species are individually bound to Fe—O sites, with only a minor fraction likely involved in ternary (Ni-Sb-Fe) surface complexation. Therefore, the inclusion of Sb—Ni paths in the fitting would not enable unambiguous resolution of Sb—Ni contributions. Therefore, the Sb—Fe coordination environment was interpreted as representative of the overall local structure.

Compared to the individual Sb(V) adsorption samples, the local coordination environment of the co-sorption samples, particularly the coordination numbers (CNs), exhibited pronounced variations. Notably, the presence of Ni^{2+} facilitated the appearance of a second Sb—Fe shell, attributed to the formation of corner-sharing complexes. Concurrently, the CNs associated with edge-sharing complexes decreased in the presence of Ni^{2+}. These observations collectively suggest that the adsorption mechanism is altered by the presence of co-existing cations, with a proportion of Sb(V) shifting from edge-sharing to corner-sharing configurations. Such changes are consistent with the likely formation of ternary surface complexes, in which Sb(V) and Ni^{2+} simultaneously interact with the iron(III) (oxyhydr)oxide surface, potentially through shared coordinating oxygen atoms. This interpretation is further supported by the observed variations in surface potential (Fig. 5), which indicate electrostatic reorganization during co-sorption. It is also consistent with previous studies reporting the formation of ternary surface complexes (e.g., Ca-Sb(V)-goethite and Ca/Mg–Sb(V)–TiO_2) on

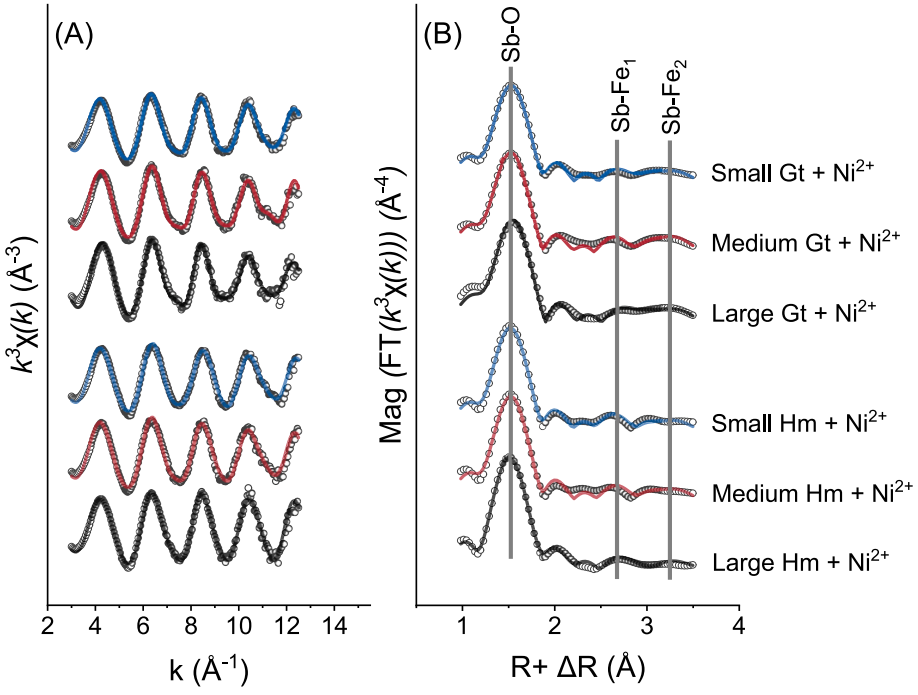

Fig. 6. Antimony K-edge k^3-weighted EXAFS spectra (A) and the corresponding Fourier Transform magnitude spectra (B) for co-sorption of Sb(V) with Ni^{2+} onto iron (III) (oxyhydr)oxide as a function of particle size. The empty symbols and solid lines show measured data and corresponding shell fits, respectively.

iron (oxyhydr)oxides and titanium oxide mineral surfaces (Kumar et al., 2025; Song et al., 2022; Shi et al., 2021; Jiang et al., 2019). Such ternary complexation may enhance both the adsorption capacity and structural stability of the surface-bound species. However, given the indirect nature of the evidence, future studies employing complementary techniques (e.g., FTIR spectroscopy and surface charge titration) as well as modeling techniques (e.g. CD-MUSIC model) are needed to further constrain and verify the formation and structure of these complexes. Overall, the results suggest the likely formation of ternary surface complexes on both goethite and hematite, irrespective of particle size.

3.4. Mechanisms of size-dependent adsorption and co-sorption behavior

Several studies have investigated the mechanisms of Sb adsorption on mineral surfaces using batch sorption experiments and EXAFS spectroscopy (Sun et al., 2023; Yan et al., 2022; Zhou et al., 2023). However, the effects of particle size and co-existing cations on Sb(V) binding mechanisms onto iron(III) (oxyhydr)oxide surfaces remain poorly understood. In this study, the integration of size-dependent adsorption and co-sorption trends from macroscopic batch experiments (Fig. 1 and Fig. 4), along with aggregation state and surface charge characterization (Fig. 2 and Fig. 5), provides a comprehensive view of how particle size and co-existing cation influence Sb(V) uptake. In combination with the identification of Sb—Fe coordination environments from EXAFS analyses (Fig. 3 and Fig. 6), these results reveal the underlying mechanisms responsible for enhanced adsorption with decreasing particle size and the synergistic effects induced by co-existing Ni^{2+} (Fig. S13).

3.4.1. Individual Sb(V) adsorption onto goethite and hematite

In the absence of Ni^{2+}, Sb(V) exhibits a higher adsorption capacity and stronger affinity toward smaller particles relative to larger particles and to goethite relative to hematite. Several factors may contribute to these observed differences, including the reactive surface area, surface charge, aggregation pattern, surface defects, Fe vacancies, and Sb—Fe binding configurations (Hou et al., 2022; Notini et al., 2018; Cwiertny et al., 2008; Liu et al., 2021). Among these, surface area has been widely recognized as a key factor controlling reactivity toward adsorption and reduction in previous studies (Cwiertny et al., 2008). However, after normalization by BET surface area, the observed trends persist, indicating that BET surface area alone cannot account for the differential adsorption capacity. Differences in surface charge may also contribute to the observed preferential adsorption capacity. In both the adsorption and co-sorption systems, $Sb(OH)_6^-$ was the predominant antimonate species at the experimental pH of 6.5, as predicted by Sb speciation distribution as a function of pH (Kumar et al., 2025). The measured points of zero charge (PZC) for the synthesized minerals indicate that all surfaces were, in principle, positively charged at pH 6.5 (SI, Fig. S8). Previous studies have extensively demonstrated that negatively charged organic molecules and anionic species adsorb onto iron(III) (oxyhydr) oxide surfaces primarily through electrostatic interactions (Liu et al., 2021). Consequently, smaller particles, which maintain more positively charged surface charge than their larger counterparts at pH 6.5, likely provide stronger electrostatic attraction and higher affinity for $Sb(OH)_6^-$, partially explaining their higher sorption of Sb compared to larger particles.

Although aggregation can influence accessible surface area, our DLS measurements (Fig. 2) indicate that it cannot fully account for the observed adsorption trends. Even under conditions of extensive aggregation, smaller particles consistently exhibited higher surface area-normalized adsorption, suggesting that their enhanced reactivity may also be attributed to intrinsic surface properties. Previous studies have shown that variations in exposed crystal facets can markedly affect the observed adsorption capacity and affinity for both contaminants and organic matter (Huang et al., 2025; Chen et al., 2025; Iqbal et al., 2024; Shen et al., 2020). In our systems, XRD patterns (SI, Fig. S1) revealed systematic changes in facet distribution with decreasing particle size. Specifically, for goethite, the relative contribution of the (110) facet decreases, while the proportion of the (111) facet increases with decreasing particle size. For hematite, the relative intensity of the dominant (104) facet decreases, whereas other facets such as (110), (113), and (116) become more prominent. The shift toward particular crystal facets with decreasing size likely enhances Sb adsorption by increasing the proportion of more reactive and high-energy surfaces. In addition, smaller particles commonly exhibit a higher density of defect sites (Notini et al., 2018), a greater abundance of undercoordinated Fe vacancies (Hou et al., 2022), and increased surface energy (Navrotsky et al., 2008). These characteristics, supported by the structural disorder and lattice distortion observed in our Mössbauer spectra and XRD patterns (Fig. S1 and S2), may contribute to the enhanced Sb(V) retention on nanoparticles.

Similar nanoparticle-driven enhancements in surface reactivity have been reported for other trace elements (Madden et al., 2006; Xiao et al., 2015; Barton et al., 2011; Waychunas and Zhang, 2008). For example, smaller hematite nanoparticles exhibit higher adsorption affinity toward Cu^{2+}, which is attributed to a greater abundance of structurally distorted, high-energy surface sites (Madden et al., 2006). Likewise, Pb^{2+} sorption to nanohematite shows subtle but distinct size-dependent effects in sorption edges, even after normalization to BET surface area (Barton et al., 2011). Collectively, these findings together with our results suggest that surface charge, specific exposed crystal facets, and intrinsic size-dependent properties, rather than surface area alone, lead to the enhanced Sb(V) uptake by smaller goethite and hematite particles in our systems.

3.4.2. Co-sorption of Sb(V) and Ni^{2+} onto goethite and hematite

The presence of the co-existing cation Ni^{2+} markedly promoted Sb (V) adsorption onto iron(III) (oxyhydr)oxides by 16 to 89%. Similar enhancements have been reported in previous co-adsorption studies with other chemical species and have been attributed to mechanisms such as increased electrostatic interactions, the formation of surface precipitates, or the likely development of ternary surface complexes (Kumar et al., 2025; Shi et al., 2021; Fan et al., 2016; Liu et al., 2021). For instance, Fan et al. (Fan et al., 2016) demonstrated that dissolved Fe^{2+} enhanced Sb(V) adsorption onto goethite through Fe(II)-Sb(V) co-precipitation. Likewise, Jiang et al. (Jiang et al., 2019) reported that Sb (V) and Ca^{2+} formed Ca(II)-Sb(V)-TiO_2 ternary complexes, facilitating Sb(V) removal from tap water. Based on our experimental findings and previous reports, we propose that the observed synergistic effect is primarily driven by enhanced electrostatic interactions, decreased aggregation state, and the likely formation of ternary surface complexes.

In our study, we found that Ni^{2+} adsorption onto Sb-modified surfaces partially neutralized the negative surface charge generated by Sb $(OH)_6^-$ adsorption (Fig. 5). This electrostatic rebalancing would reduce repulsion between $Sb(OH)_6^-$ and the negatively charged surface, thereby facilitating additional Sb(V) uptake. The observed differences in surface charge between samples reacted with Sb(V) alone and those reacted with Sb(V) and Ni^{2+} further confirm Ni^{2+} adsorption and may indicate the potential formation of ternary surface complexes. In addition, iron(III) (oxyhydr)oxide reacted with Sb(V) and Ni^{2+} displayed slight shifts toward smaller aggregate sizes compared to their controls (SI, Fig. S9). Decreased aggregation may decrease physical occlusion of reactive sites and increase pore throat accessibility within aggregates, thereby improving Sb(V) adsorption capacity.

EXAFS shell-fitting analysis at the Sb K-edge revealed that co-sorption with Ni^{2+} introduced an additional Sb—Fe shell at longer distances (~3.52–3.55 Å), which were attributed to corner-sharing coordination geometry (Burton et al., 2019; Mitsunobu et al., 2010). The presence of both edge-sharing and corner-sharing configurations under co-sorption conditions suggests a structural rearrangement of Sb binding in response to Ni^{2+}. Although an explicit Sb—Ni path could not be resolved in the fits due to nearly identical backscattering amplitudes and phase shifts of Fe and Ni and the limited sensitivity of Sb EXAFS to Ni

neighbors, the combined evidence supports Ni(II) participation in ternary complex formation. This evidence includes (i) coordination changes observed in EXAFS fits, (ii) partial neutralization of surface charge in zeta potential measurements, and (iii) prior reports of divalent cation-facilitated ternary complexation (Kumar et al., 2025; Shi et al., 2021; Fan et al., 2016; Liu et al., 2021). We therefore propose that the synergistic enhancement in Sb(V) uptake observed in co-sorption experiments is also driven by the likely formation of Ni-Sb-Fe ternary surface complexes.

3.5. Environmental implications

Iron(III) (oxyhydr)oxide nanoparticles are ubiquitous in various environmental and geological settings (Hochella Jr et al., 2008; Cornell and Schwertmann, 2003; Hochella Jr et al., 2019). Their physicochemical properties, including surface reactivity, are strongly size-dependent (Gilbert and Banfield, 2005). In contaminated environments, Sb(V) frequently co-occurs with other cations such as Ni^{2+}, Pb^{2+}, and Ca^{2+}, particularly in mining-impacted soils and waters (Khan et al., 2019; Jurkovič et al., 2019; Palmer et al., 2015). Therefore, elucidating the relationships among particle size, mineral type, co-existing cations, and sorption mechanisms that govern antimony behavior advances our understanding of its long-term retention and potential remobilization under dynamic aqueous geochemical conditions.

Our findings show that nanoscale iron(III) (oxyhydr)oxides exhibit high Sb(V) adsorption capacities, ranging from 1.1 to 2.3 μmol/m^2, suggesting that these particles can serve as highly effective sorbents in natural waters. Under similar conditions, bentonite, δ-MnO_2 and hydrous Al oxide exhibited lower adsorption capacities (< 1 μmol/m^2) (Sun et al., 2018; Ilgen and Trainor, 2012; Xi et al., 2011), whereas Mn-oxides achieved the highest values, reaching up to 2.6 μmol/m^2 (Liu et al., 2015). Notably, when size effects are considered, our nanoscale iron(III) (oxyhydr)oxide particles still demonstrate adsorption capacities comparable to, and in most cases exceeding, those of common mineral sorbents. However, contaminant retention models for natural systems typically emphasize adsorption capacity of different mineral types, without incorporating size-dependent particle distribution and adsorption capacity. To illustrate the importance of particle size effects, Sb(V) retention was modeled assuming a total Fe concentration of 10 g/L, representative of Fe-rich sediment suspensions in natural aquatic systems (Kappler et al., 2021). The model considered particle size fractions of 1–10 nm, 10–100 nm, and > 100 nm, with relative particle number abundance estimated using Pareto's power law distribution (Ranville and Montano, 2015; Westerhoff et al., 2018). Applying experimental adsorption capacities for each size range, we estimated Sb(V) retention contributions and found that excluding particles < 0.45 μm (typical size separated in field filtration) can lead to substantial underestimation of Sb retention, by factors of 35 for goethite and 7 for hematite (SI, Fig. S14). Because small nanoparticles are highly mobile and susceptible to redox transformations, their presence can facilitate long-distance transport and influence the geochemical cycling and mobility of Sb in natural environments. These findings highlight the need for advanced analytical approaches, such as field-flow fractionation (FFF) and single-particle inductively coupled plasma mass spectrometry (spICP-MS), which enable more accurate detection and characterization of nanoparticles, thereby allowing particle size effects to be explicitly considered in contaminant transport and risk assessment models. It should also be noted that the present model is based on a simplified particle size distribution and does not explicitly account for particle aggregation or competitive adsorption by natural organic matter and other anions (e.g., phosphate). These factors may significantly influence the accessibility and reactivity of mineral surfaces under natural conditions (Huang et al., 2025; Verbeeck et al., 2019). In addition, competitive interactions among co-existing anions may alter Sb(V) binding mechanisms and surface complexation behavior. Future model development should therefore incorporate Sb retention behavior in more complex environmental systems, including aggregation dynamics, interactions with organic matter, and competitive sorption with co-existing anions, to improve predictions of Sb retention and transport in natural and engineered environmental settings.

Beyond individual adsorption, co-sorption with Ni^{2+} significantly enhanced Sb(V) retention, likely through synergistic mechanisms involving electrostatic interactions and potential ternary surface complex formation. This implies that in multi-contaminant systems, cation-anion interactions at mineral interfaces could promote stronger contaminant retention than predicted from single-element pollution models, a factor often overlooked in risk assessment and remediation design. Notably, the enhancement induced by Ni^{2+} was more pronounced in smaller particle fractions (Fig. 4), where the high surface reactivity facilitates the formation of ternary Ni-Sb-Fe complexes. These nanoscale interactions not only increase the overall adsorption capacity but also strengthen the binding between Sb(V) and iron(III) (oxyhydr) oxide surfaces, thereby decreasing the likelihood of Sb remobilization under fluctuating environmental conditions. It is important to note that the mechanisms observed here, enhanced electrostatic interactions, decreased aggregation, and additional likely ternary surface complex formation, are mostly applicable to other redox-inactive divalent cations (e.g., Zn^{2+}, Ca^{2+}, Cd^{2+}, Pb^{2+}) that commonly co-occur with Sb in mining-impacted settings (Khan et al., 2019; Jurkovič et al., 2019; Palmer et al., 2015; Trois et al., 2007). Consequently, incorporating the effects of co-existing divalent cations into size-resolved adsorption models is essential for accurately predicting Sb partitioning, transport, and long-term stability in natural and engineered systems.

In addition, these results support the potential application of nanoparticulate goethite and hematite in engineered systems for Sb(V) and other trace element removal. In practice, such materials can be introduced as sorbent media in wastewater treatment units, permeable reactive barriers, or mine tailing remediation reactors, where they immobilize contaminants through surface complexation and potential co-precipitation. However, environmental deployment warrants caution. Seasonal and hydrological variations, such as fluctuating water tables, oxic–anoxic cycling, and pH shifts near mining tailings, may destabilize adsorbed species, potentially triggering Sb remobilization. Future work should therefore investigate the long-term stability of Sb(V) adsorbed on iron(III) (oxyhydr)oxides under dynamic geochemical conditions, including competition from other anions (e.g., phosphate, sulfate), interactions with natural organic matter, and microbially mediated Fe(III) mineral reduction. While these factors are beyond the scope of the present work, such investigations are essential for predicting the in-situ performance and sustainability of iron(III) (oxyhydr) oxide nanoparticles in contaminant remediation.

CRediT authorship contribution statement

Xiyang Xu: Writing – original draft, Investigation, Funding acquisition, Formal analysis, Data curation, Conceptualization. **Biao Wan:** Writing – review & editing, Methodology, Conceptualization. **Kerstin Hockmann:** Writing – review & editing, Methodology, Funding acquisition, Data curation. **Valerie A. Schoepfer:** Writing – review & editing, Funding acquisition, Data curation. **Andreas Kappler:** Writing – review & editing, Supervision, Resources, Project administration, Funding acquisition. **Muammar Mansor:** Writing – review & editing, Supervision, Project administration, Methodology, Funding acquisition, Conceptualization. **Prachi Joshi:** Writing – review & editing, Supervision, Project administration, Methodology, Funding acquisition, Conceptualization.

Declaration of competing interest

The authors declare the following financial interests/personal relationships which may be considered as potential competing interests:

Andreas Kappler reports financial support was provided by German

Research Foundation. Xiyang Xu reports financial support was provided by Chinese Scholarship Council. Prachi Joshi reports equipment, drugs, or supplies was provided by Canadian Light Source Inc. Prachi Joshi reports equipment, drugs, or supplies was provided by ESRF. Reports a relationship with that includes: Has patent pending to. If there are other authors, they declare that they have no known competing financial interests or personal relationships that could have appeared to influence the work reported in this paper.

Acknowledgements

We thank Franziska Schaedler and Lars Grimm for their technical support in the lab, Tsz Ho Chiu for BET surface area measurements, and Carolin L. Dreher for micro-XRD measurements. Antimony XAS measurements were conducted at the Canadian Light Synchrotron (CLS), (grant No. 39G13933) and at the European Synchrotron Radiation Facility (ESRF) (grant No. EV-584). We are grateful to Jeremiah Shuster for his assistance with SEM measurements, to Sandra Richter, Rebecca Stahl, and Lorenz Henneberg for their assistance with TEM measurements, also to Center for Molecular Biology of Plants (ZMBP) for their support. The authors gratefully acknowledge the Tübingen Structural Microscopy Core Facility (funded by the Federal Ministry of Education and Research (BMBF) and the Baden-Württemberg Ministry of Science as part of the Excellence Strategy of the German Federal and State Governments) for their support & assistance in this work. We also thank the German Research Foundation DFG (INST 37/1027-1 FUGG) for financial support. This research was supported by the CSC scholarship (202106010075).

Appendix A. Supplementary data

Details about synthesis and characterization of nanoparticulate goethite; modelling of Sb and Ni adsorption isotherms; Sb K-edge XANES and EXAFS measurements and data analysis (PDF). Supplementary data to this article can be found online at https://doi.org/10.1016/j.chemgeo.2026.123428.

Data availability

All data displayed in the figures is available at Mendeley Data (https://data.mendeley.com/datasets/st6rgdh7w6).

References

Ankudinov, A.L., Ravel, B., Rehr, J., Conradson, S., 1998. Real-space multiple-scattering calculation and interpretation of x-ray-absorption near-edge structure. Phys. Rev. B 58, (12), 7565.
Arai, Y., 2008. Spectroscopic evidence for Ni (II) surface speciation at the iron oxyhydroxides–water interface. Environ. Sci. Technol. 42 (4), 1151–1156.
Barker, A.J., Mayhew, L., Douglas, T., Ilgen, A., Trainor, T., 2020. Lead and antimony speciation associated with the weathering of bullets in a historic shooting range in Alaska. Chem. Geol. 553, 119797.
Barton, L.E., Grant, K.E., Kosel, T., Quicksall, A.N., Maurice, P.A., 2011. Size-dependent Pb sorption to nanohematite in the presence and absence of a microbial siderophore. Environ. Sci. Technol. 45 (8), 3231–3237.
Berlepsch, P., Armbruster, T., Brugger, J., Criddle, A., Graeser, S., 2003. Tripuhyite, FeSbO4, revisited. Mineral. Mag. 67 (1), 31–46.
Burton, E.D., Hockmann, K., Karimian, N., Johnston, S.G., 2019. Antimony mobility in reducing environments: the effect of microbial iron (III)-reduction and associated secondary mineralization. Geochim. Cosmochim. Acta 245, 278–289.
Chen, P., Prange, M.P., Song, D., Lee, S., Lee, S.S., Liu, J., Zhao, Y., Wang, X., Engelhard, M.H., Zhou, Y., 2025. Facet-dependent adsorption of Pb (II) on hematite (001),(116), and (104) surfaces. Environ. Sci. Technol. 59 (23), 11862–11874.
Cornell, R.M., Schwertmann, U., 2003. The Iron Oxides: Structure, Properties, Reactions, Occurrences, and Uses, vol. 664. Wiley-VCH, Weinheim.
Cwiertny, D.M., Handler, R.M., Schaefer, M.V., Grassian, V.H., Scherer, M.M., 2008. Interpreting nanoscale size-effects in aggregated Fe-oxide suspensions: reaction of Fe (II) with goethite. Geochim. Cosmochim. Acta 72 (5), 1365–1380.
Fan, J.-X., Wang, Y.-J., Fan, T.-T., Dang, F., Zhou, D.-M., 2016. Effect of aqueous Fe (II) on Sb (V) sorption on soil and goethite. Chemosphere 147, 44–51.
Filella, M., Belzile, N., Chen, Y.-W., 2002a. Antimony in the environment: a review focused on natural waters: I. Occurrence. Earth-Sci. Rev. 57 (1–2), 125–176.
Filella, M., Belzile, N., Chen, Y.-W., 2002b. Antimony in the environment: a review focused on natural waters: II. Relevant solution chemistry. Earth-Sci. Rev. 59 (1–4), 265–285.
Filella, M., Williams, P.A., Belzile, N., 2009a. Antimony in the environment: knowns and unknowns. Environ. Chem. 6 (2), 95–105.
Filella, M., Philippo, S., Belzile, N., Chen, Y., Quentel, F., 2009b. Natural attenuation processes applying to antimony: A study in the abandoned antimony mine in Goesdorf, Luxembourg. Sci. Total Environ. 407 (24), 6205–6216.
Freundlich, H., 1907. Über die adsorption in lösungen. J. Phys. Chem. 57 (1), 385–470.
Funke, H., Scheinost, A., Chukalina, M., 2005. Wavelet analysis of extended x-ray absorption fine structure data. Phys. Rev. B Condens. Matter Mater. Phys. *71*, (9), 094110.
Gilbert, B., Banfield, J.F., 2005. Molecular-scale processes involving nanoparticulate minerals in biogeochemical systems. Rev. Mineral. Geochem. 59 (1), 109–155.
Gunawardene, O., Gunathilake, C., Amaraweera, A., Fernando, N., Manipura, A., Manamperi, W., Kulatunga, K., Rajapaksha, S., Gamage, A., Dassanayake, R., 2021. Removal of Pb (II) ions from aqueous solution using modified starch. J. Compos. Sci. *5*, (2), 46.
Guo, X., Wu, Z., He, M., Meng, X., Jin, X., Qiu, N., Zhang, J., 2014. Adsorption of antimony onto iron oxyhydroxides: adsorption behavior and surface structure. J. Hazard. Mater. 276, 339–345.
Hall, K.R., Eagleton, L.C., Acrivos, A., Vermeulen, T., 1966. Pore-and solid-diffusion kinetics in fixed-bed adsorption under constant-pattern conditions. Ind. Eng. Chem. Fundam. 5 (2), 212–223.
He, M., Wang, N., Long, X., Zhang, C., Ma, C., Zhong, Q., Wang, A., Wang, Y., Pervaiz, A., Shan, J., 2019. Antimony speciation in the environment: recent advances in understanding the biogeochemical processes and ecological effects. J. Environ. Sci. 75, 14–39.
Hochella Jr., M.F., 2002. Nanoscience and technology: the next revolution in the Earth sciences. Earth Planet. Sci. Lett. 203 (2), 593–605.
Hochella Jr., M.F., Lower, S.K., Maurice, P.A., Penn, R.L., Sahai, N., Sparks, D.L., Twining, B.S., 2008. Nanominerals, mineral nanoparticles, and earth systems. Science 319 (5870), 1631–1635.
Hochella Jr., M.F., Mogk, D.W., Ranville, J., Allen, I.C., Luther, G.W., Marr, L.C., McGrail, B.P., Murayama, M., Qafoku, N.P., Rosso, K.M., 2019. Natural, incidental, and engineered nanomaterials and their impacts on the earth system. Science 363, (6434) eaau8299.
Hou, J., Tan, X., Xiang, Y., Zheng, Q., Chen, C., Sha, Z., Ren, L., Wang, M., Tan, W., 2022. Insights into the underlying effect of Fe vacancy defects on the adsorption affinity of goethite for arsenic immobilization. Environ. Pollut. 314, 120268.
Huang, Y., Zhao, X., Yang, B., Tang, Y., Zhou, D., Gu, X., 2025. A simple geochemical model for predicting Sb (v) partitioning: from iron oxides to complex soil systems. J. Hazard. Mater. 496, 139191.
Hummel, W., Curti, E., 2003. Nickel aqueous speciation and solubility at ambient conditions: a thermodynamic elegy. Monatsh. Chem. 134, 941–973.
Ilgen, A.G., Trainor, T.P., 2012. Sb (III) and Sb (V) sorption onto Al-rich phases: hydrous Al oxide and the clay minerals kaolinite KGa-1b and oxidized and reduced nontronite NAu-1. Environ. Sci. Technol. 46 (2), 843–851.
Iqbal, M., Zhang, K., Davranche, M., Dia, A., Dutruch, L., Vantelon, D., Ratié, G., Maxit, B., Hanna, K., Marsac, R., 2024. Facet-dependent adsorption of rare earth elements (REEs) and actinides onto goethite: REE pattern variability and cerium anomaly. Environ. Sci. Technol. 58 (49), 21729–21739.
Jiang, Y., Yan, L., Nie, X., Yan, W., 2019. Remediation of antimony-contaminated tap water using granular TiO2 column. Environ. Chem. 17 (4), 323–331.
Jurkovič, Ľ., Majzlan, J., Hiller, E., Klimko, T., Voleková-Lalinská, B., Méres, Š., Göttlicher, J., Steininger, R., 2019. Natural attenuation of antimony and arsenic in soils at the abandoned Sb-deposit Poproč, Slovakia. Environ. Earth Sci. *78*, (24), 672.
Kappler, A., Bryce, C., Mansor, M., Lueder, U., Byrne, J.M., Swanner, E.D., 2021. An evolving view on biogeochemical cycling of iron. Nat. Rev. Microbiol. 19 (6), 360–374.
Khan, U.A., Kujala, K., Nieminen, S.P., Räisänen, M.L., Ronkanen, A.-K., 2019. Arsenic, antimony, and nickel leaching from northern peatlands treating mining influenced water in cold climate. Sci. Total Environ. 657, 1161–1172.
Kumar, R., Jing, C., Yan, L., 2025. A critical review on arsenic and antimony adsorption and transformation on mineral facets. J. Environ. Sci. 153, 56–75.
Langmuir, I., 1918. The adsorption of gases on plane surfaces of glass, mica and platinum. J. Am. Chem. Soc. 40 (9), 1361–1403.
Liu, H., Chen, T., Frost, R.L., 2014. An overview of the role of goethite surfaces in the environment. Chemosphere 103, 1–11.
Liu, R., Xu, W., He, Z., Lan, H., Liu, H., Qu, J., Prasai, T., 2015. Adsorption of antimony (V) onto Mn (II)-enriched surfaces of manganese-oxide and FeMn binary oxide. Chemosphere 138, 616–624.
Liu, J., Zhu, R., Ma, L., Fu, H., Lin, X., Parker, S.C., Molinari, M., 2021. Adsorption of phosphate and cadmium on iron (oxyhydr) oxides: a comparative study on ferrihydrite, goethite, and hematite. Geoderma 383, 114799.
Madden, A.S., Hochella Jr., M.F., 2005. A test of geochemical reactivity as a function of mineral size: Manganese oxidation promoted by hematite nanoparticles. Geochim. Cosmochim. Acta 69 (2), 389–398.
Madden, A.S., Hochella Jr., M.F., Luxton, T.P., 2006. Insights for size-dependent reactivity of hematite nanomineral surfaces through Cu2+ sorption. Geochim. Cosmochim. Acta 70 (16), 4095–4104.
Majzlan, J., Lalinská, B., Chovan, M., Bläß, U., Brecht, B.R., Göttlicher, J.R., Steininger, R., Hug, K., Ziegler, S., Gescher, J., 2011. A mineralogical, geochemical, and microbiogical assessment of the antimony-and arsenic-rich neutral mine drainage tailings near Pezinok, Slovakia. Am. Mineral. 96 (1), 1–13.

Martinelli, A., Ferretti, M., Buscaglia, V., Cabella, R., Lucchetti, G., 2002. Formation and decomposition of the rutile-type compound FeSbO 4. J. Therm. Anal. Calorim. 70 (1), 123–127.
Mitsunobu, S., Takahashi, Y., Terada, Y., Sakata, M., 2010. Antimony (V) incorporation into synthetic ferrihydrite, goethite, and natural iron oxyhydroxides. Environ. Sci. Technol. 44 (10), 3712–3718.
Mitsunobu, S., Muramatsu, C., Watanabe, K., Sakata, M., 2013. Behavior of antimony (V) during the transformation of ferrihydrite and its environmental implications. Environ. Sci. Technol. 47 (17), 9660–9667.
Murad, E., Cashion, J., 2011. Mössbauer Spectroscopy of Environmental Materials and their Industrial Utilization. Springer Science & Business Media.
Navrotsky, A., Mazeina, L., Majzlan, J., 2008. Size-driven structural and thermodynamic complexity in iron oxides. Science 319 (5870), 1635–1638.
Notini, L., Latta, D.E., Neumann, A., Pearce, C.I., Sassi, M., N'Diaye, A.T., Rosso, K.M., Scherer, M.M., 2018. The role of defects in Fe (II)–goethite electron transfer. Environ. Sci. Technol. 52 (5), 2751–2759.
Palmer, K., Ronkanen, A.-K., Kløve, B., 2015. Efficient removal of arsenic, antimony and nickel from mine wastewaters in Northern treatment peatlands and potential risks in their long-term use. Ecol. Eng. 75, 350–364.
Ranville, J., Montano, M.D., 2015. Size distributions. In: Frontiers of Nanoscience, 8. Elsevier, pp. 91–121.
Ravel, B., Newville, M., 2005. ATHENA, ARTEMIS, HEPHAESTUS: data analysis for X-ray absorption spectroscopy using IFEFFIT. J. Synchrotron Radiat. 12 (4), 537–541.
Rehr, J., Mustre de Leon, J., Zabinsky, S., Albers, R., 1991. Theoretical X-ray absorption fine structure standards. J. Am. Chem. Soc. 113 (14), 5135–5140.
Ritchie, V.J., Ilgen, A.G., Mueller, S.H., Trainor, T.P., Goldfarb, R.J., 2013. Mobility and chemical fate of antimony and arsenic in historic mining environments of the Kantishna Hills district, Denali National Park and Preserve, Alaska. Chem. Geol. 335, 172–188.
Sari, A., Tuzen, M., Citak, D., Soylak, M., 2007. Equilibrium, kinetic and thermodynamic studies of adsorption of Pb (II) from aqueous solution onto Turkish kaolinite clay. J. Hazard. Mater. 149 (2), 283–291.
Shen, Z., Zhang, Z., Li, T., Yao, Q., Zhang, T., Chen, W., 2020. Facet-dependent adsorption and fractionation of natural organic matter on crystalline metal oxide nanoparticles. Environ. Sci. Technol. 54 (14), 8622–8631.
Shi, M., Min, X., Ke, Y., Lin, Z., Yang, Z., Wang, S., Peng, N., Yan, X., Luo, S., Wu, J., 2021. Recent progress in understanding the mechanism of heavy metals retention by iron (oxyhydr) oxides. Sci. Total Environ. 752, 141930.
Song, K., Zhang, C., Shan, J., Wang, W., Liu, H., He, M., 2022. Adsorption behavior and surface complexation modeling of oxygen anion Sb (V) adsorption on goethite. Sci. Total Environ. 833, 155284.
Sun, Q., Liu, C., Alves, M.E., Ata-Ul-Karim, S.T., Zhou, D.-M., He, J.-Z., Cui, P.-X., Wang, Y.-J., 2018. The oxidation and sorption mechanism of Sb on δ-MnO2. Chem. Eng. J. 342, 429–437.
Sun, Q., Liu, C., Fan, T., Cheng, H., Cui, P., Gu, X., Chen, L., Ata-Ul-Karim, S.T., Zhou, D., Wang, Y., 2023. A molecular level understanding of antimony immobilization mechanism on goethite by the combination of X-ray absorption spectroscopy and density functional theory calculations. Sci. Total Environ. 865, 161294.
Trois, C., Marcello, A., Pretti, S., Trois, P., Rossi, G., 2007. The environmental risk posed by small dumps of complex arsenic, antimony, nickel and cobalt sulphides. J. Geochem. Explor. 92 (1), 83–95.
Verbeeck, M., Warrinnier, R., Gustafsson, J.P., Thiry, Y., Smolders, E., 2019. Soil organic matter increases antimonate mobility in soil: an Sb (OH) 6 sorption and modelling study. Appl. Geochem. 104, 33–41.
Verbeeck, M., Moens, C., Gustafsson, J.P., 2021. Mechanisms of antimony ageing in soils: an XAS study. Appl. Geochem. 128, 104936.
Von Der Heyden, B., Roychoudhury, A., Myneni, S., 2019. Iron-rich nanoparticles in natural aquatic environments. Minerals *9*, (5), 287.
Waychunas, G.A., Zhang, H., 2008. Structure, chemistry, and properties of mineral nanoparticles. Elements 4 (6), 381–387.
Westerhoff, P., Atkinson, A., Fortner, J., Wong, M.S., Zimmerman, J., Gardea-Torresdey, J., Ranville, J., Herckes, P., 2018. Low risk posed by engineered and incidental nanoparticles in drinking water. Nat. Nanotechnol. 13 (8), 661–669.
Wilson, S.C., Lockwood, P.V., Ashley, P.M., Tighe, M., 2010. The chemistry and behaviour of antimony in the soil environment with comparisons to arsenic: a critical review. Environ. Pollut. 158 (5), 1169–1181.
Xi, J., He, M., 2013. Removal of Sb (III) and Sb (V) from aqueous media by goethite. Water Qual. Res. J. Can. 48 (3), 223–231.
Xi, J., He, M., Lin, C., 2011. Adsorption of antimony (III) and antimony (V) on bentonite: Kinetics, thermodynamics and anion competition. Microchem. J. 97 (1), 85–91.
Xiao, Q., Sun, Y., Zhang, J., Li, Q., 2015. Size-dependent of chromium (VI) adsorption on nano α-Fe2O3 surface. Appl. Surf. Sci. 356, 18–23.
Xu, X., Mansor, M., Li, G., Chiu, T.H., Haderlein, S.B., Kappler, A., Joshi, P., 2025. Size-dependent reduction kinetics of iron oxides in single and mixed mineral systems. Environ. Sci. Technol. 59 (5), 2519–2530.
Xu, X., Joshi, P., Hockmann, K., Dreher, C.L., Schoepfer, V., Tung, P.-Y., Walmsley, J.C., Kappler, A., Mansor, M., 2026. Antimony coprecipitation suppresses microbial reduction of goethite and hematite and limits Sb release across particle sizes. Geochim. Cosmochim. Acta. 417, 135–149.
Yan, L., Chan, T., Jing, C., 2022. Mechanistic study for antimony adsorption and precipitation on hematite facets. Environ. Sci. Technol. 56 (5), 3138–3146.
Zhou, W., Zhou, J., Feng, X., Wen, B., Zhou, A., Liu, P., Sun, G., Zhou, Z., Liu, X., 2023. Antimony isotope fractionation revealed from EXAFS during adsorption on Fe (oxyhydr) oxides. Environ. Sci. Technol. 57 (25), 9353–9361.